Supplementary Information

Ferrocenyl helquats: unusual chiral organometallic nonlinear optical chromophores

Laura E. R. Buckley,[a] Benjamin J. Coe,[a] Daniela Rusanova,[a] Sergio Sánchez,[a] Michael Jirásek,[b] Vishwas D. Joshi,[b] Jan Vávra,[b] Dushant Khobragade,[b] Lubomír Pospíšil,[c] Šárka Ramešová,[c] Ivana Císařová,[d] David Šaman,[b] Radek Pohl,[b] Koen Clays,[e] Nick Van Steerteghem,[e] Bruce S. Brunschwig[f] and Filip Teplý[b]

[a] *School of Chemistry, University of Manchester, Oxford Road, Manchester M13 9PL, UK.*
[b] *The Institute of Organic Chemistry and Biochemistry of the Czech Academy of Sciences, Flemingovo n. 542/2, 166 10 Prague 6, Czech Republic.*
[c] *J. Heyrovský Institute of Physical Chemistry of the Czech Academy of Sciences, 18223 Prague 8, Czech Republic*
[d] *Department of Inorganic Chemistry, Charles University, Hlavova 2030/8, 128 43 Prague 2, Czech Republic*
[e] *Department of Chemistry, University of Leuven, Celestijnenlaan 200 D, B-3001, Belgium*
[f] *Molecular Materials Research Center, Beckman Institute, MC 139-74, California Institute of Technology, 1200 East California Boulevard, Pasadena, California 91125, United States*

1. Crystallographic Study

Table S1 Crystallographic data and refinement details for salt [1][PF_6]$_2$

empirical formula	$C_{32}H_{28}F_{12}FeN_2P_2$
fw	786.35
cryst system	triclinic
space group	$P\bar{1}$
a/Å	11.4717(4)
b/Å	11.7174(4)
c/Å	13.2142(5)
α/deg	70.568(1)
β/deg	75.978(1)
γ/deg	79.815(1)
U/Å^3	1616.13(10)
Z	2
T/K	150(2)
μ/mm^{-1}	0.662
cryst size/mm	0.80 × 0.34 × 0.12
cryst description	metallic dark blue-violet plate
reflns collected	26013
independent reflns (R_{int})	7422 (0.0254)
θ_{max}/deg (completeness)	27.50 (99.9)
reflns with $I > 2\sigma(I)$	6108
GOF on F^2	1.025
final $R1$, $wR2$ [$I > 2\sigma(I)$]	0.0375, 0.0873
(all data)	0.0511, 0.0933
peak and hole/eÅ^{-3}	0.60, –0.42

2. Spectroscopic Studies

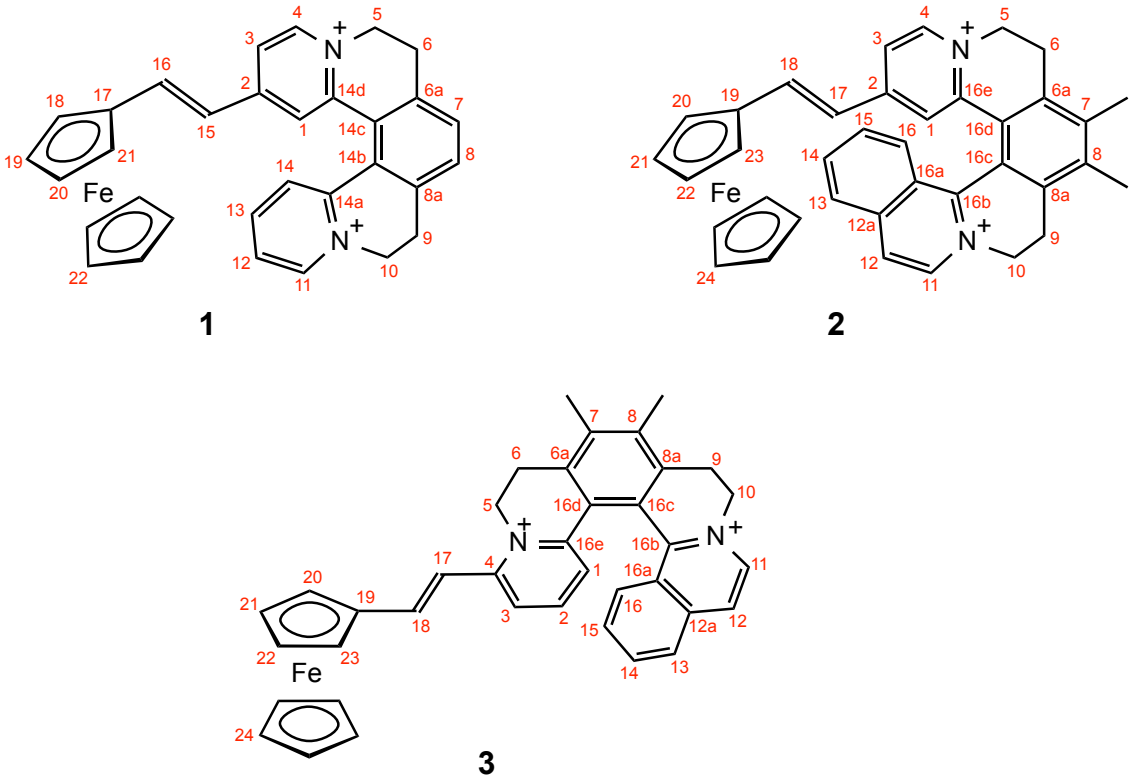

Fig. S1 C-atom numbering schemes used to assign the NMR signals for complexes **1**–**3**.

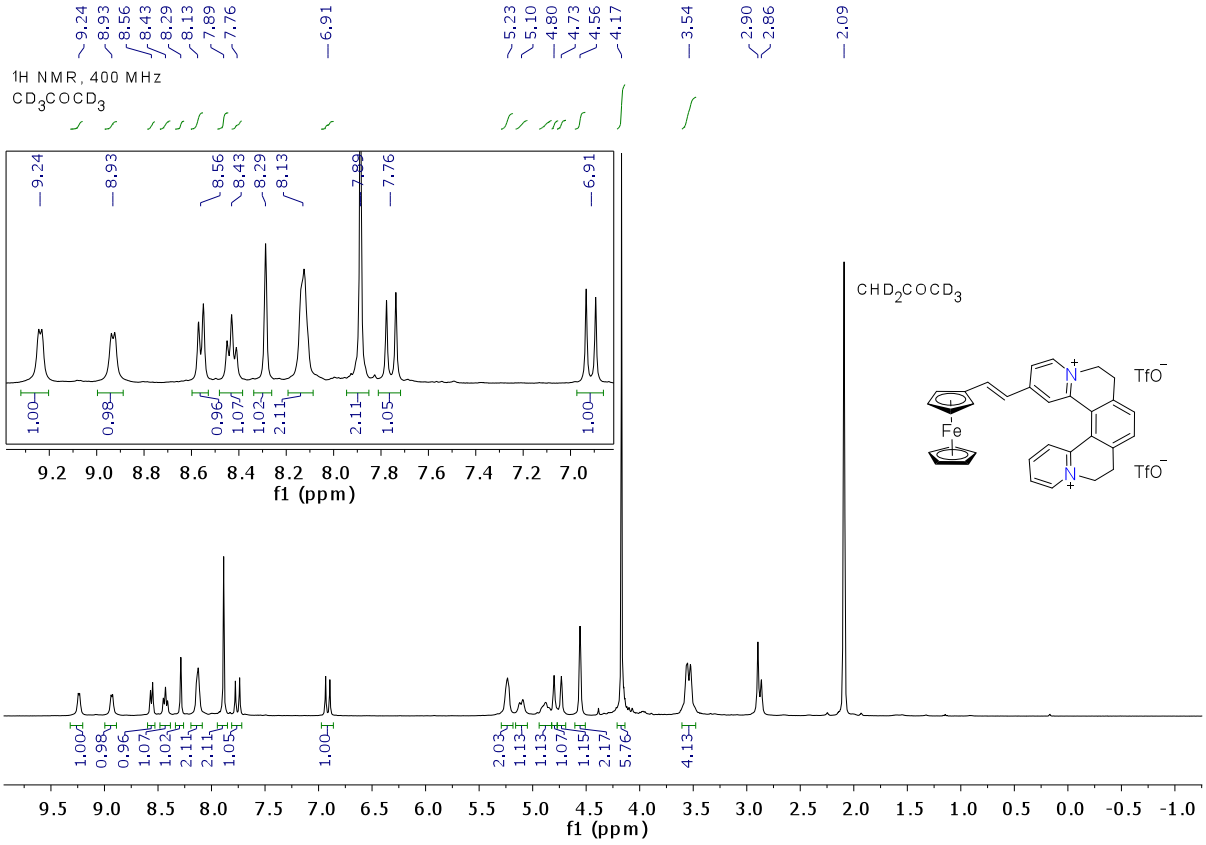

Fig. S2 ^{1}H NMR spectrum of complex salt [**1**][TfO]$_2$ (400 MHz, CD_3COCD_3).

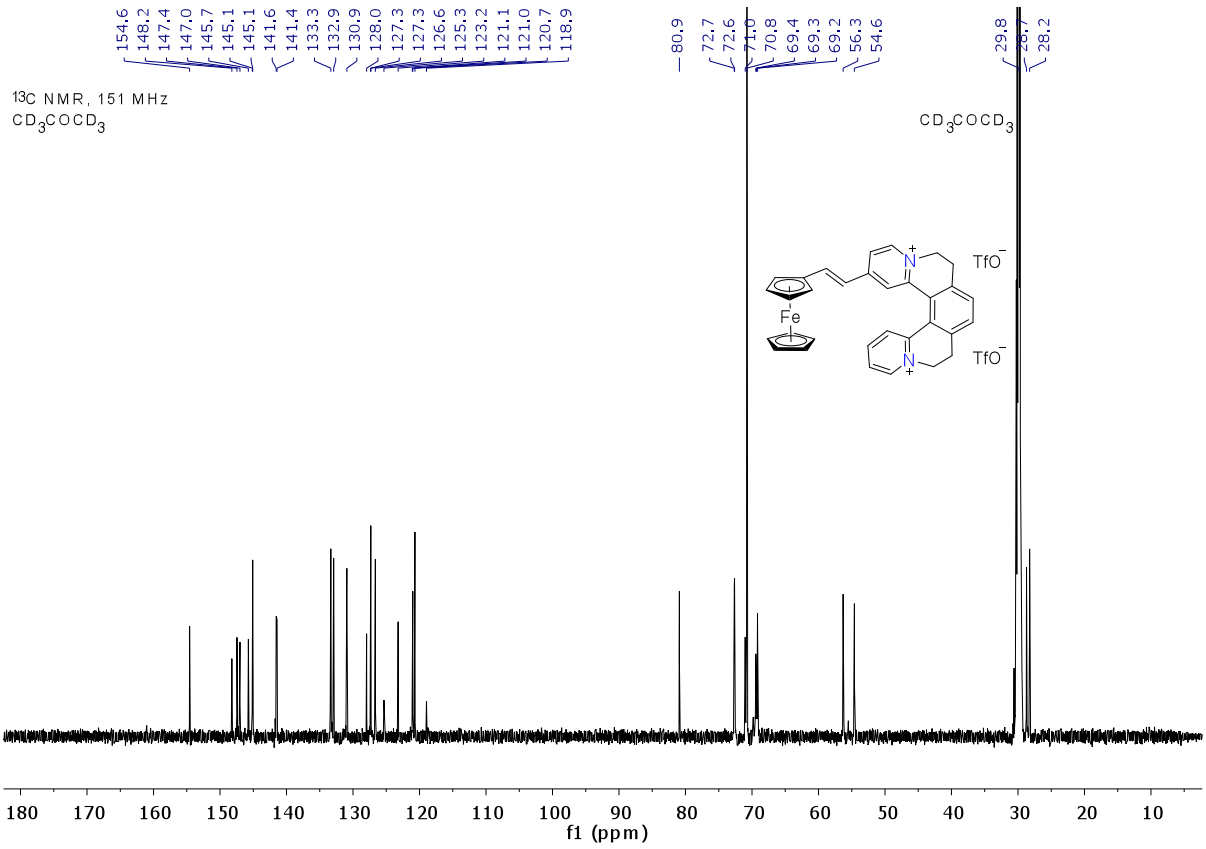

Fig. S3 ^{13}C NMR spectrum of complex salt [**1**][TfO]$_2$ (151 MHz, CD_3COCD_3).

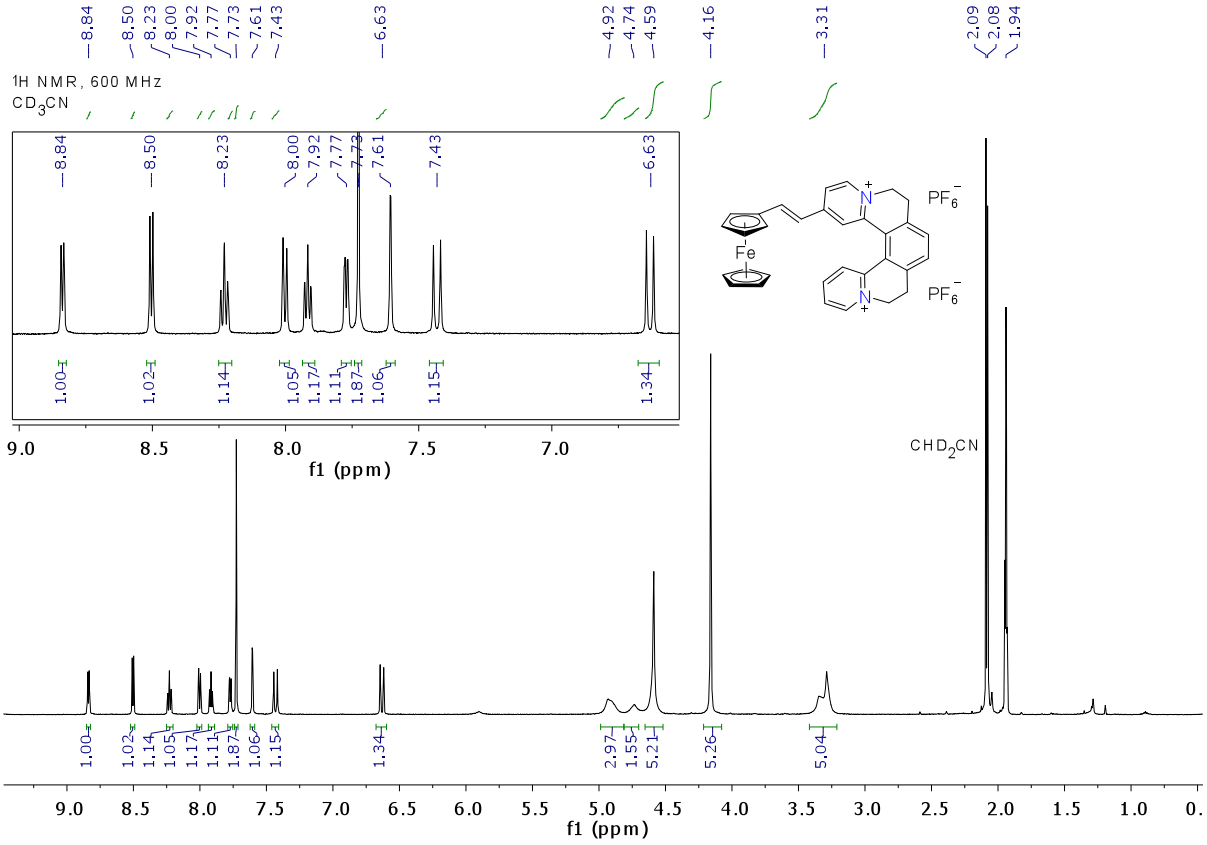

Fig. S4 ^{1}H NMR spectrum of complex salt [**1**][PF_6]$_2$ (600 MHz, CD_3CN).

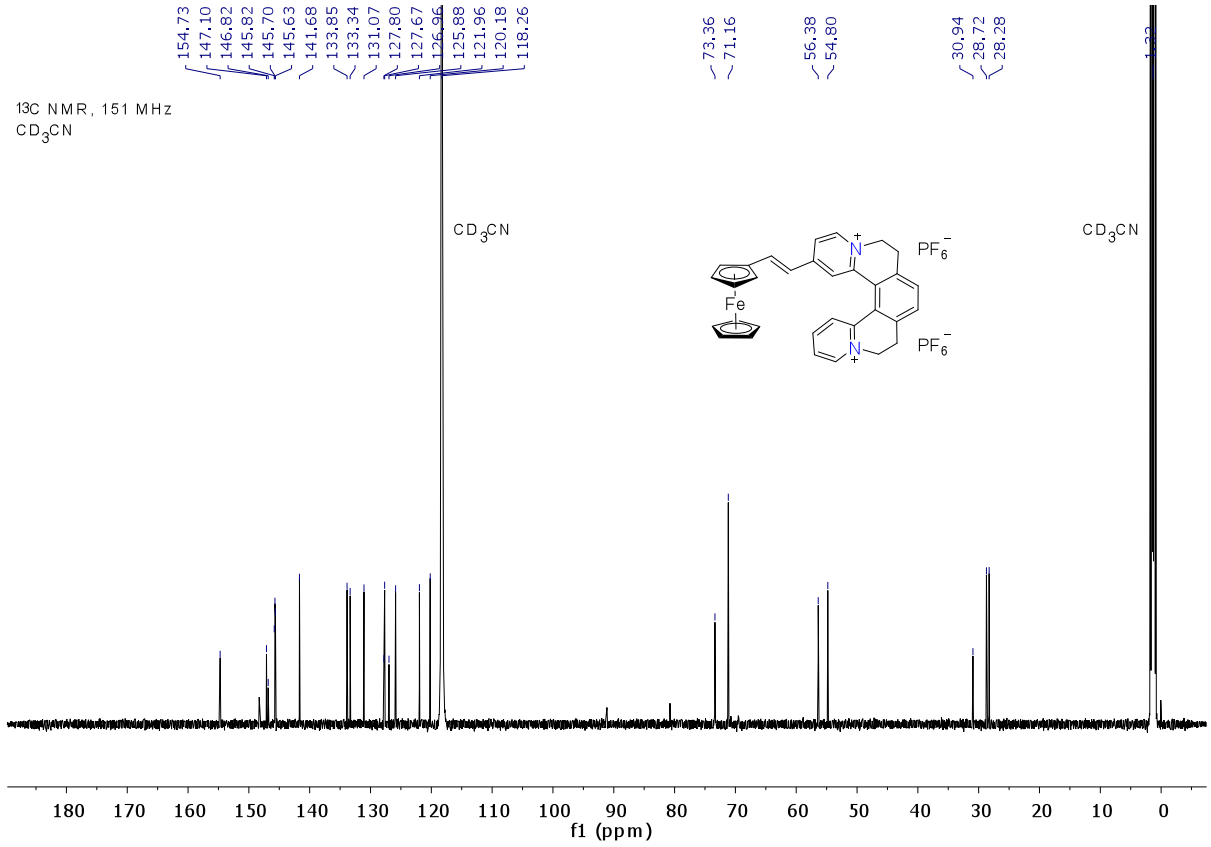

Fig. S5 ^{13}C NMR spectrum of complex salt [**1**][PF_6]$_2$ (151 MHz, CD_3CN).

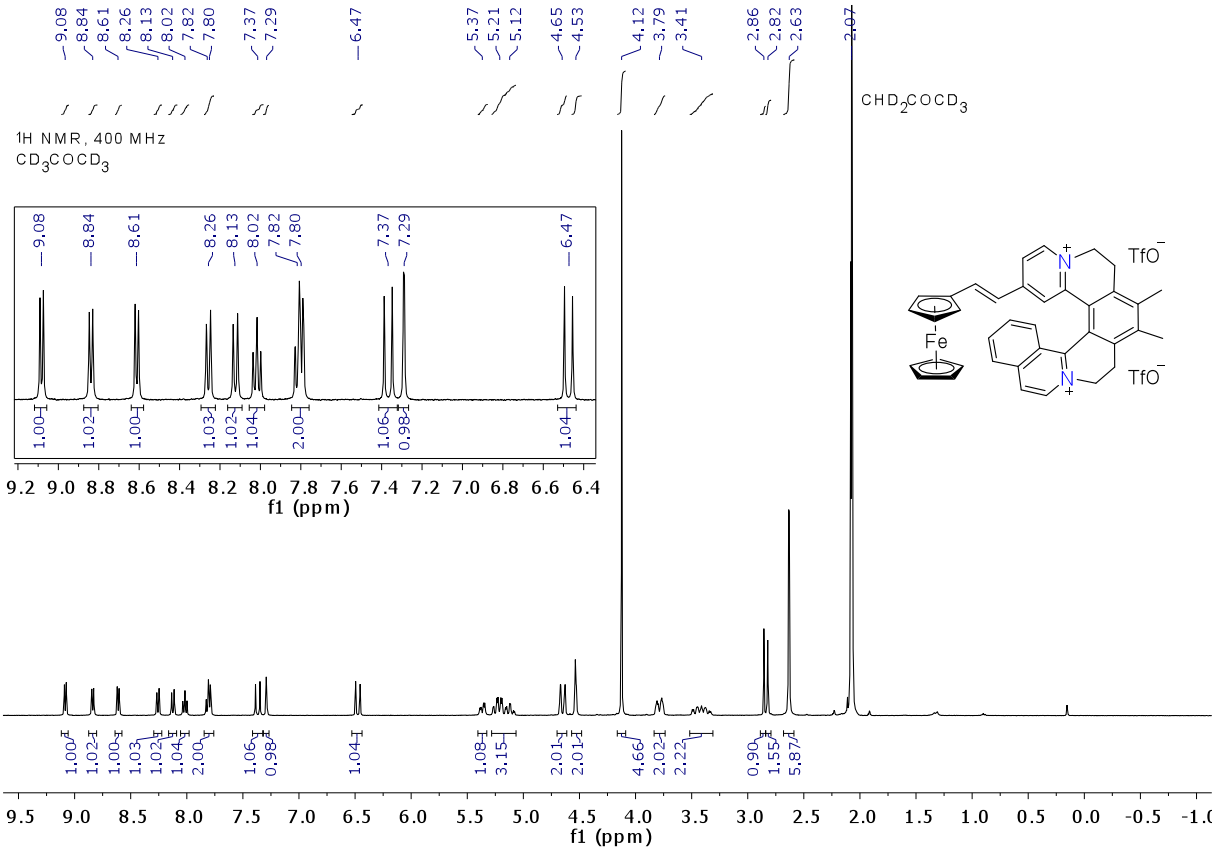

Fig. S6 ^{1}H NMR spectrum of complex salt [**2**][TfO]$_2$ (400 MHz, CD_3COCD_3).

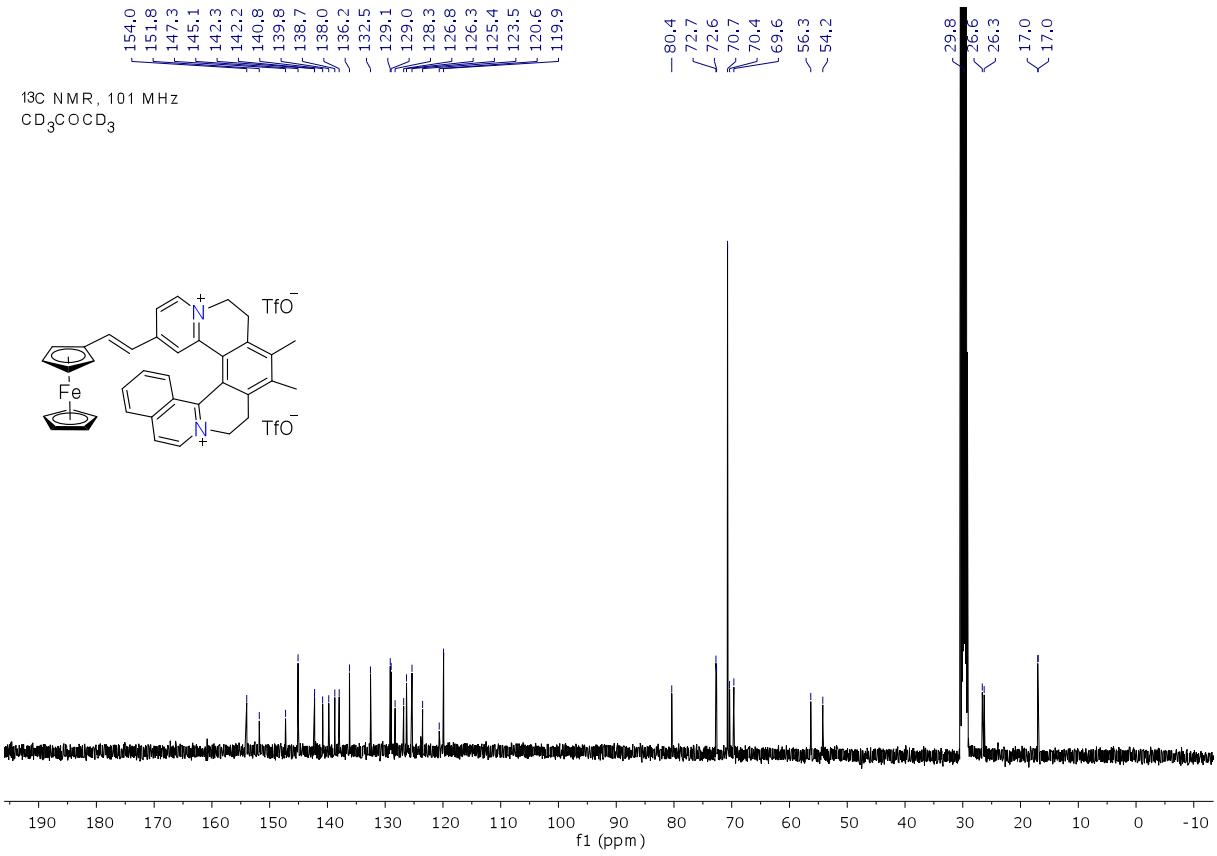

Fig. S7 ^{13}C NMR spectrum of complex salt [**2**][TfO]$_2$ (101 MHz, CD_3COCD_3).

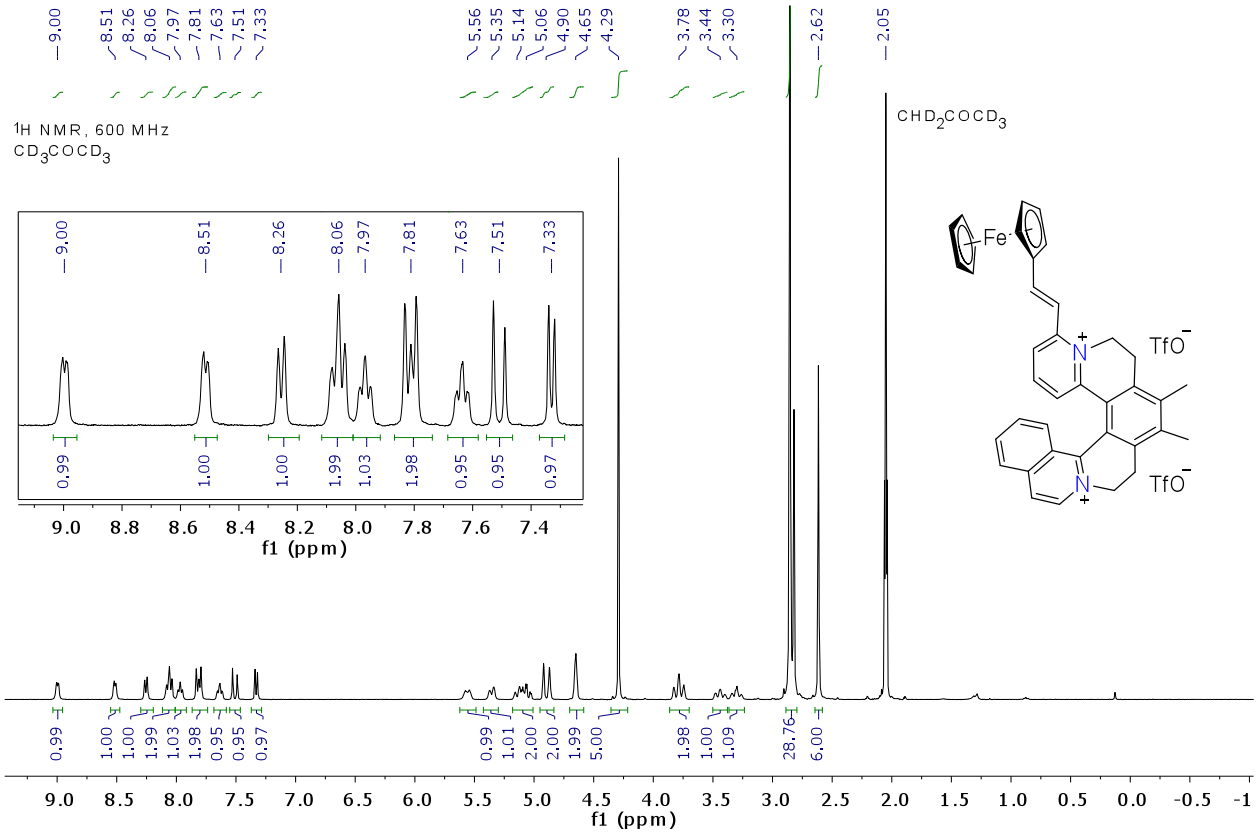

Fig. S8 ^{1}H NMR spectrum of complex salt [**3**][TfO]$_2$ (400 MHz, CD_3COCD_3).

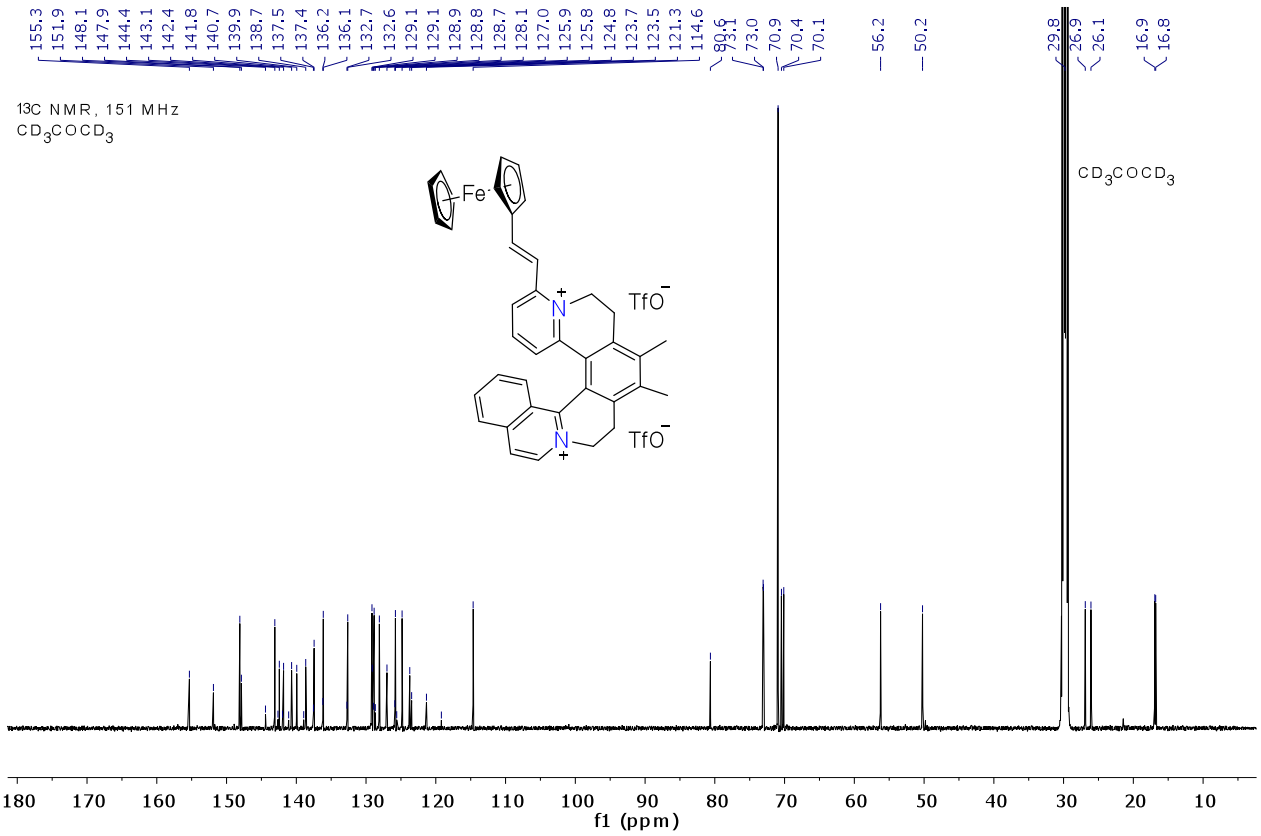

Fig. S9 ^{13}C NMR spectrum of complex salt [**3**][TfO]$_2$ (101 MHz, CD_3COCD_3).

3. Electrochemical Studies

The presence of three reversible one-electron processes is evidenced by cyclic voltammetry, and also polarographic waves and their log-plot analysis, and by phase-sensitive AC polarography. The latter also confirms a strong adsorption, which produces a post-wave following the second reduction step. Besides that, adsorption yields an imaginary Faradaic admittance component much higher than its real counterpart. Typical electrochemical data are shown in Figures S10–S12. All of the salts [**1**–**3**][TfO]$_2$ give almost identical curve shapes, with difference noticeable only in the appearance of the adsorption post-wave.

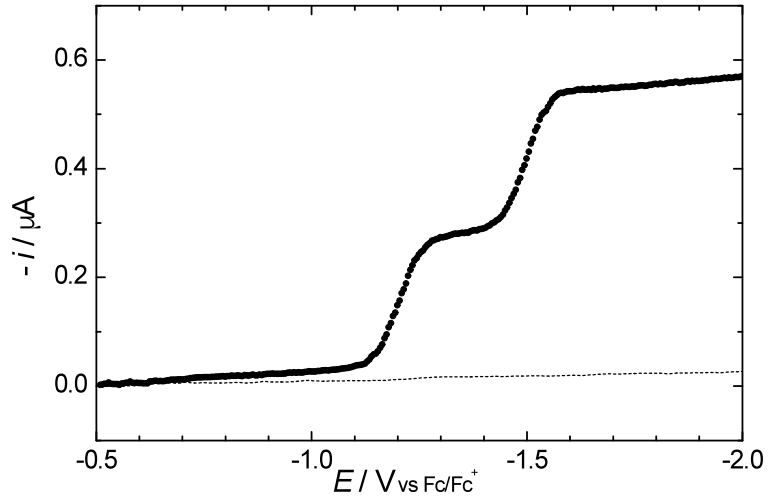

Fig. S10 DC polarogram of 0.2 mM [**3**][TfO]$_2$ and 0.1 M [N(C$_4$H$_9$-*n*)$_4$]PF$_6$ in MeCN. The dotted line is the blank.

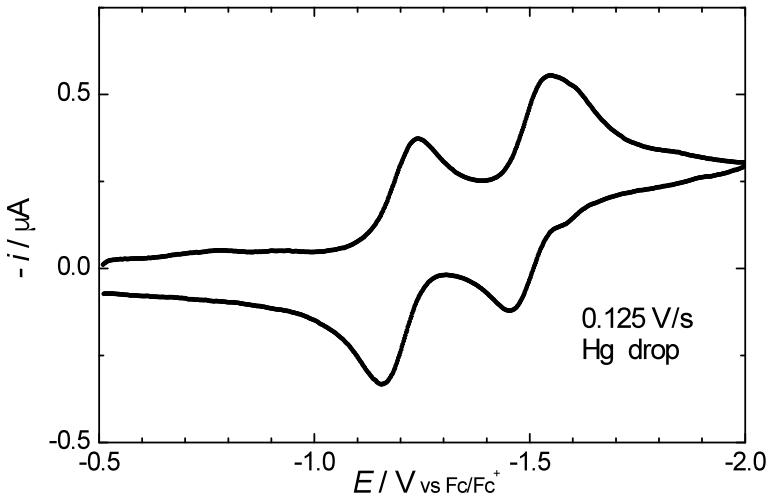

Fig. S11 Cyclic voltammogram of the reductive region of 0.2 mM [**3**][TfO]$_2$ and 0.1 M [N(C$_4$H$_9$-*n*)$_4$]PF$_6$ in MeCN using a Hg-drop electrode at a scan rate of 125 mV s^{-1}.

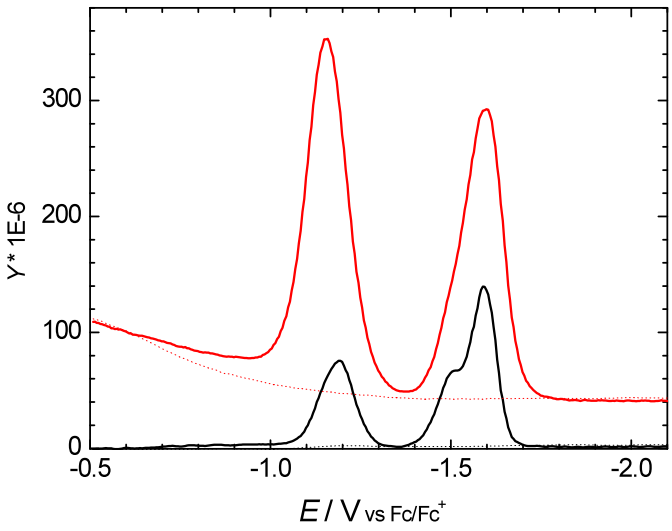

Fig. S12 The phase-sensitive AC polarogram of the reductive region of 0.2 mM [**3**][TfO]$_2$ and 0.1 M [N(C_4H_9-*n*)$_4$]PF_6 in MeCN using a Hg-drop electrode ; black curve = real admittance component ; red curves = imaginary admittance component. The dotted lines are the blank. The frequency and amplitude of the superimposed sine wave voltage were 160 Hz and 10 mV (p-p).

4. Theoretical Studies

Table S2 Selected TD-DFT-calculated data for the complexes 1–3[a]

complex	no.	E (eV)	λ (nm)	f_{os}	major contributions
1	1	2.04	607	0.101	H → L (36%), H → L+1 (12%), H → L+7 (16%)
	2	2.43	510	0.039	H–3 → L+7 (15%), H–1 → L+6 (39%)
	3	2.63	471	0.108	H → L (56%), H → L+7 (10%)
	4	2.88	430	0.106	H–2 → L (58%), H–1 → L+6 (21%)
	5	3.14	395	0.486	H–2 → L (25%), H → L+1 (55%)
	6	3.36	369	0.062	H–3 → L (18%), H–2 → L+1 (11%), H–1 → L+6 (12%), H → L+1 (15%), H → L+7 (15%)
	7	3.52	352	0.087	H → L+2 (89%)
	8	3.59	345	0.051	H–3 → L+6 (22%), H–1 → L+7 (14%), H → L+6 (16%)
	9	3.59	345	0.164	H–3 → L (22%), H–2 → L+1 (39%)
	10	3.63	342	0.070	H–5 → L (86%)
	11	3.69	336	0.193	H–6 → L (43%), H–4 → L (42%)
	12	3.70	335	0.174	H–6 → L (41%), H–4 → L (45%)
	13	3.78	328	0.031	H–3 → L (20%), H–3 → L+7 (12%), H–2 → L+1 (23%)
	14	4.03	308	0.032	H–7 → L (82%)
	15	4.08	304	0.033	H–2 → L+2 (67%), H → L+3 (11%)
	16	4.26	291	0.025	H–5 → L+1 (82%), H → L+3 (12%)
	17	4.29	289	0.112	H–6 → L+1 (84%)
	18	4.64	267	0.011	H–6 → L+2 (61%), H → L+4 (11%)
	19	4.66	266	0.125	H–5 → L+2 (48%), H → L+4 (28%)
	20	4.68	265	0.030	H–7 → L+1 (26%), H–5 → L+2 (24%), H–3 → L+2 (18%), H–2 → L+3 (11%)
	21	5.14	241	0.044	H–10 → L (46%), H → L+5 (13%)
	22	5.17	240	0.014	H–10 → L (28%), H–2 → L+4 (22%), H → L+5 (15%)
	23	5.21	238	0.016	H–7 → L+2 (87%)
	24	5.39	230	0.145	H–11 → L (14%), H–6 → L+3 (27%), H–3 → L+3 (16%)
	25	5.39	230	0.099	H–6 → L+3 (12%), H–3 → L+3 (18%), H → L+8 (31%)
	26	5.39	230	0.071	H–5 → L+3 (23%), H → L+8 (35%)
2	1	2.06	602	0.093	H → L (29%), H → L+1 (16%), H → L+7 (20%)
	2	2.45	507	0.036	H–4 → L+7 (18%), H–1 → L+6 (40%)
	3	2.59	479	0.057	H → L (61%), H → L+1 (10%)
	4	2.88	431	0.015	H–2 → L (40%), H–1 → L+6 (23%), H → L+1 (19%)
	5	3.03	409	0.459	H–2 → L (36%), H → L+1 (42%)
	6	3.25	382	0.291	H–3 → L (87%)

	7	3.30	376	0.159	H–2 → L+1 (29%), H–1 → L+6 (13%), H → L+7 (12%)
	8	3.40	365	0.081	H–5 → L (90%)
	9	3.51	353	0.234	H–4 → L (28%), H–2 → L+1 (50%)
	10	3.69	336	0.094	H → L+2 (73%)
	11	3.72	333	0.030	H–4 → L (26%), H–3 → L+1 (27%)
	12	3.75	331	0.061	H–3 → L+1 (67%)
	13	3.80	326	0.039	H–8 → L (77%), H–7 → L (10%)
	14	3.90	318	0.066	H–5 → L+1 (81%)
	15	3.96	313	0.051	H → L+3 (89%)
	16	4.01	309	0.034	H–7 → L (30%), H–4 → L+1 (42%)
	17	4.26	291	0.049	H–2 → L+2 (79%)
	18	4.32	287	0.011	H–10 → L (21%), H–8 → L+1 (13%), H–3 → L+2 (42%)
	19	4.37	284	0.031	H–8 → L+1 (65%)
	20	4.51	275	0.022	H–10 → L (14%), H–3 → L+2 (21%), H–3 → L+3 (13%), H–2 → L+3 (39%)
	21	4.53	274	0.034	H–10 → L (16%), H–3 → L+2 (14%), H–3 → L+3 (10%), H–2 → L+3 (46%)
	22	4.64	267	0.095	H–5 → L+2 (72%)
	23	4.71	263	0.019	H → L+5 (65%)
	24	4.79	259	0.092	H–12 → L (18%), H–10 → L (25%), H–3 → L+3 (33%)
	25	4.92	252	0.040	H–12 → L (23%), H–10 → L+1 (15%), H–5 → L+3 (45%)
	26	4.94	251	0.062	H–12 → L (31%), H–11 → L (38%), H–5 → L+3 (20%)
	27	4.96	250	0.060	H–12 → L (13%), H–11 → L (27%), H–8 → L+2 (28%), H–3 → L+3 (14%)
	28	5.00	248	0.036	H–11 → L (25%), H–10 → L+1 (20%), H–8 → L+2 (15%), H–5 → L+3 (26%)
	29	5.14	241	0.042	H–2 → L+5 (43%), H–2 → L+6 (16%)
	30	5.21	238	0.222	H–10 → L+1 (20%), H–8 → L+2 (20%), H–8 → L+3 (18%)
3	1	2.09	593	0.053	H–1 → L+6 (14%), H → L (11%), H → L+1 (23%), H → L+7 (24%)
	2	2.45	506	0.018	H–4 → L+1 (10%), H–4 → L+7 (19%), H–1 → L+6 (42%)
	3	2.65	467	0.099	H → L (79%)
	4	2.95	421	0.028	H–2 → L (28%), H–1 → L+6 (18%), H → L+1 (24%)
	5	3.05	407	0.447	H–2 → L (53%), H → L+1 (25%)
	6	3.28	378	0.092	H–3 → L (26%), H–2 → L+1 (15%), H → L+1 (10%), H → L+2 (15%)
	7	3.30	376	0.256	H–3 → L (65%), H → L+1 (10%)
	8	3.50	354	0.387	H–2 → L+1 (53%), H → L+2 (37%)
	9	3.56	348	0.011	H–5 → L (63%), H → L+2 (10%)
	10	3.85	322	0.024	H–3 → L+1 (77%)
	11	3.85	322	0.034	H–8 → L (21%), H–7 → L (13%), H–6 → L (35%), H–3 → L+1 (13%)

12	3.86	321	0.026	H–8 → L (33%), H–7 → L (20%), H–6 → L (35%)
13	3.94	315	0.072	H–2 → L+2 (81%)
14	4.20	295	0.016	H–7 → L (14%), H–6 → L (11%), H–6 → L+1 (45%), H–3 → L+2 (11%)
15	4.38	283	0.017	H–10 → L (27%), H–5 → L+2 (14%), H–3 → L+3 (28%), H–2 → L+3 (14%)
16	4.41	281	0.066	H–8 → L+1 (12%), H–7 → L+1 (20%), H–5 → L+2 (34%)
17	4.49	276	0.014	H–2 → L+3 (62%)
18	4.51	275	0.099	H–7 → L+1 (47%), H–5 → L+2 (17%), H–2 → L+3 (10%)
19	4.56	272	0.059	H–8 → L+1 (60%), H–5 → L+2 (18%)
20	4.81	258	0.084	H–11 → L (11%), H–10 → L (31%), H–8 → L+2 (12%), H–3 → L+3 (26%)
21	4.84	256	0.070	H–10 → L (10%), H–8 → L+2 (35%), H–7 → L+2 (22%)
22	4.92	252	0.090	H → L+5 (66%)
23	4.96	250	0.164	H–11 → L (45%), H–5 → L+3 (15%), H–3 → L+3 (12%)
24	5.00	248	0.063	H–11 → L (13%), H–5 → L+3 (65%)
25	5.04	246	0.019	H–8 → L+2 (25%), H–7 → L+2 (43%)
26	5.12	242	0.026	H–10 → L+1 (19%), H–8 → L+3 (17%), H–2 → L+4 (18%)

[a] Geometry optimizations and TD-DFT calculations used the PBE0 functional with the 6-311++G(d)/LANL2DZ mixed basis set, and a CPCM MeCN solvent model was included for TD-DFT. Only the transitions with $f_{os} \geq 0.01$ are included. H = HOMO, L = LUMO.

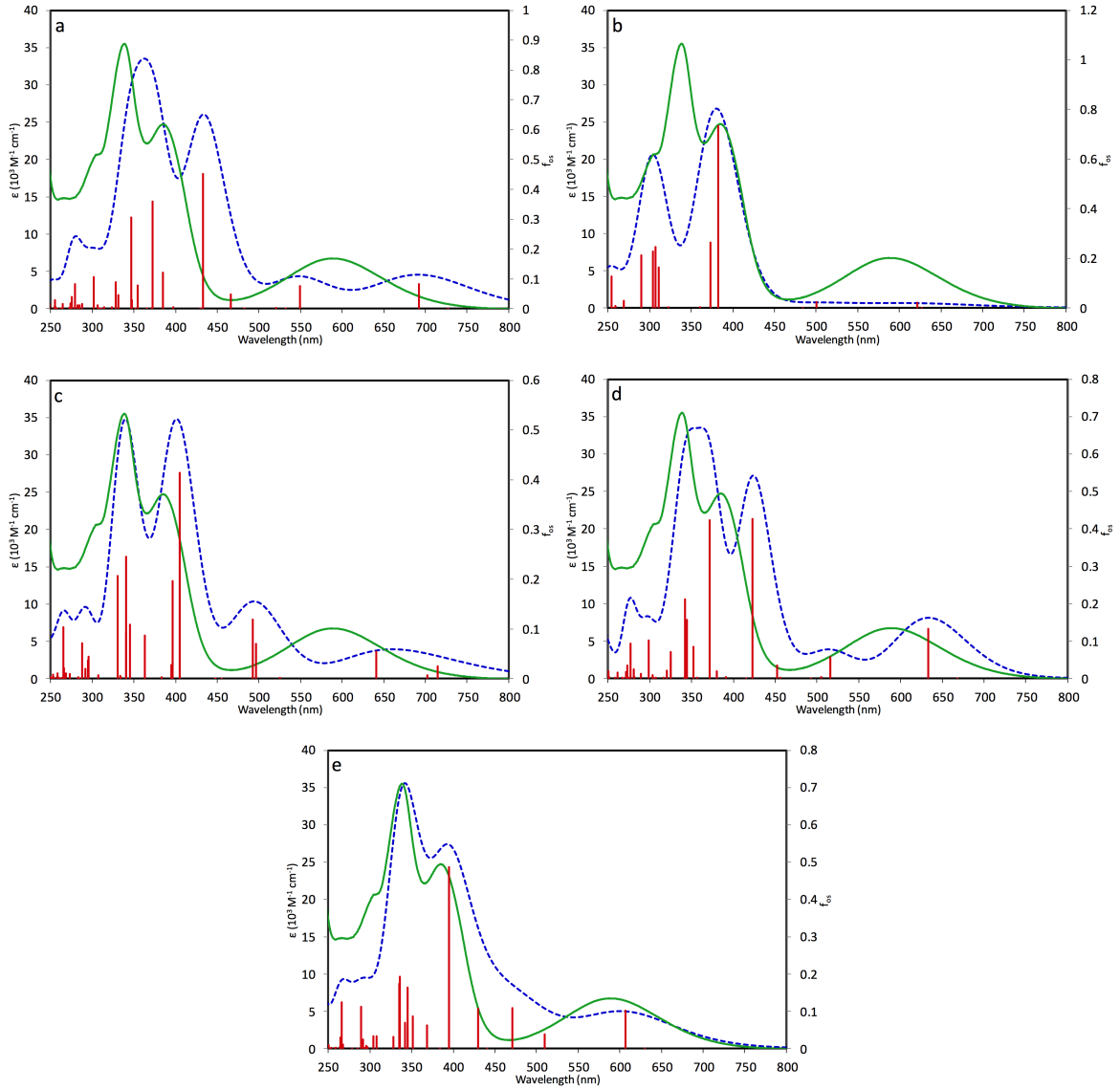

Fig. S13 Experimental UV–vis spectrum of [**1**][TfO]$_2$ (green) together with the TD–DFT–calculated spectra for complex **1** in MeCN (blue dashed), using the mixed basis set 6-311++G(d)/LANL2DZ and the functional B3LYP (a), CAM–B3LYP (b), M06 (c), BPW91 (d) or PBE0 (e). The ε–axes refer to the experimental data only and the vertical axes of the calculated data are scaled to match the main experimental absorptions. The f_{os}-axes refer to the individual calculated transitions (red).

Table S3 Geometric parameters for complex 1 from X–ray crystallography and the PBE0/6-311++G(d)/LANL2DZ-optimised structure

distances (Å)			angles (°)		
	X-ray	DFT		X-ray	DFT
C1–C2	1.44	1.42	C1–C2–C3	124.9	126.4
C2–C3	1.34	1.37	C2–C3–C4	125.1	124.8
C3–C4	1.45	1.42	C3–C4–C5	124.5	124.7
C4–C5	1.40	1.42	C4–C5–C6	119.9	120.4
C5–C6	1.36	1.36	C5–C6–N1	121.7	122.4
C6–N1	1.35	1.36	C6–N1–C9	123.5	120.5
N1–C7	1.36	1.37	N1–C9–C10	107.7	108.5
C7–C8	1.38	1.38	C9–C10–C11	109.5	109.1
C4–C8	1.40	1.42	C10–C11–C16	122.4	121.4
N1–C9	1.49	1.47	C11–C16–C15	120.6	120.7
C9–C10	1.52	1.51	C16–C15–C14	120.7	120.3
C10–C11	1.50	1.50	C15–C14–C17	121.5	121.4
C11–C12	1.40	1.40	C14–C17–C18	109.4	109.1
C7–C12	1.48	1.48	C17–C18–N2	108.8	108.4
C12–C13	1.42	1.42	C18–N2–C23	119.7	119.6
C13–C14	1.40	1.40	N2–C23–C22	121.2	121.3
C14–C15	1.40	1.39	C23–C22–C21	118.9	118.3
C15–C16	1.38	1.38	C22–C21–C20	119.0	119.7
C11–C16	1.39	1.39	C21–C20–C19	121.1	121.0
C14–C17	1.51	1.50	C20–C19–C13	123.6	123.6
C17–C18	1.51	1.51	C19–C13–C12	123.1	123.4
C18–N2	1.49	1.48	C13–C12–C7	123.4	123.8
N2–C19	1.36	1.36	C12–C7–C8	123.2	123.4
C13–C19	1.48	1.47	C7–C8–C4	121.6	122.9
C19–C20	1.39	1.40	C8–C4–C3	118.4	120.0
C20–C21	1.38	1.38	θ	51.4	60.3
C21–C22	1.39	1.39			
C22–C23	1.37	1.37			
C23–N2	1.35	1.35			

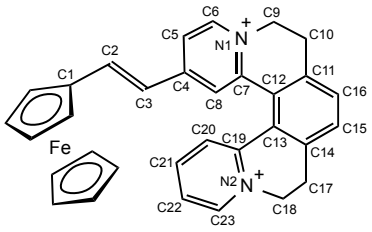

In many cases, the agreement between the theoretical and experimental geometric parameters is excellent. The differences between the bond distances are no more than 0.03 Å, while the largest difference for the bond angles is 3° for C6–N1–C9. However, the computed dihedral angle between the two pyridinium rings of the Hq fragment θ is overestimated by almost 9°.

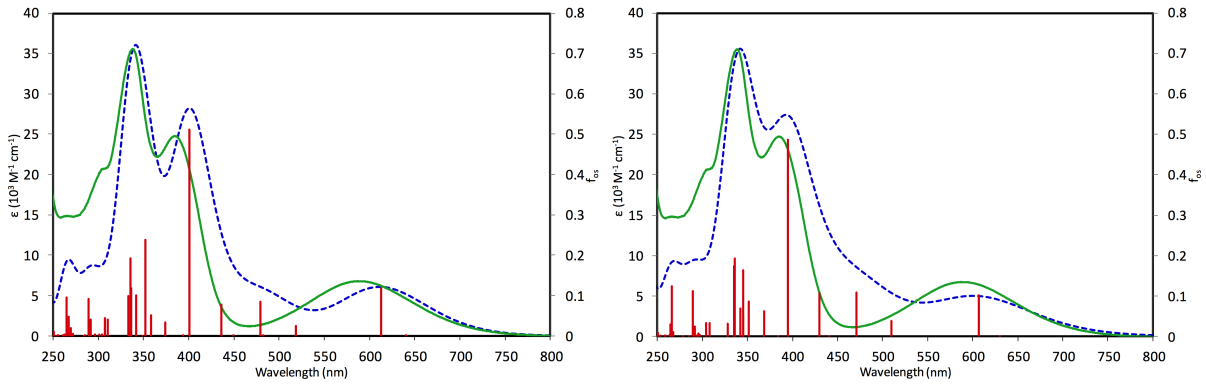

Fig. S14 Experimental UV–vis spectrum of [**1**][TfO]$_2$ (green) together with the TD–DFT–calculated spectrum for complex **1** (blue dashed) using PBE0/6-311++G(d) without the LANL2DZ pseudopotential (left) and with the pseudopotential on Fe (right).

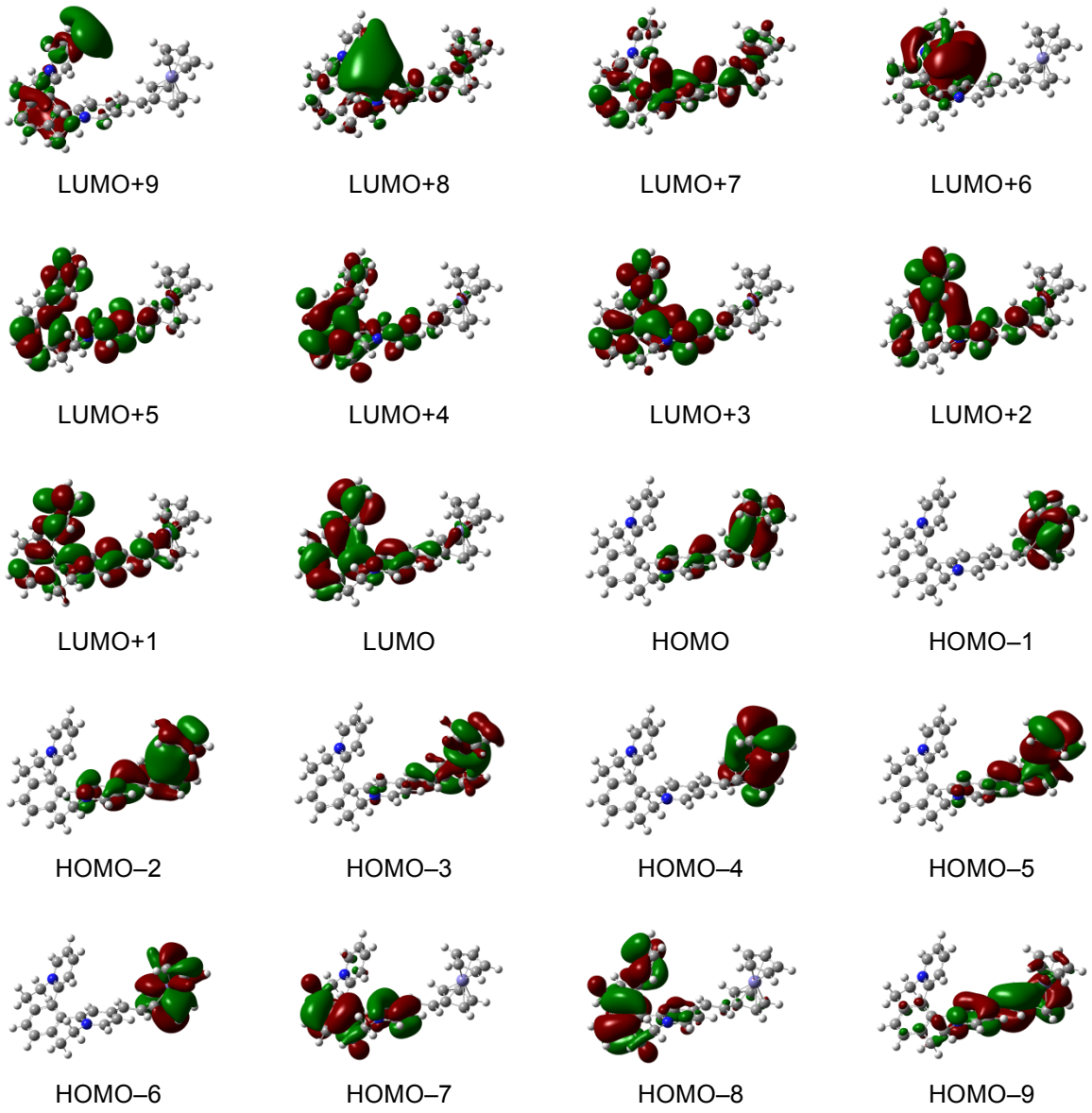

Fig. S15 PBE0/6-311++G(d)/LANL2DZ-derived contour surface diagrams of selected MOs for complex **1** (isosurface value 0.03 au).

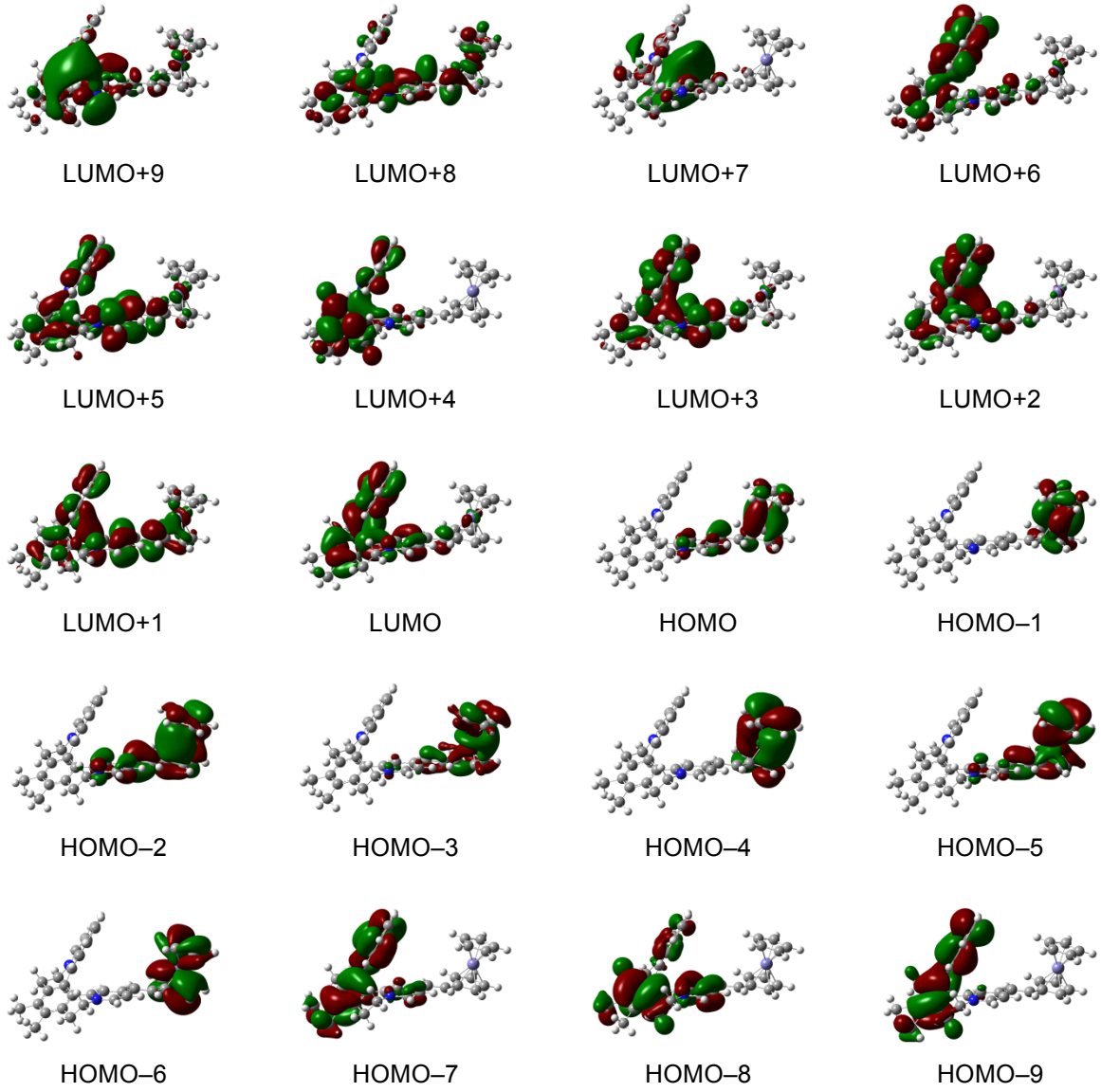

Fig. S16 PBE0/6-311++G(d)/LANL2DZ-derived contour surface diagrams of selected MOs for complex **2** (isosurface value 0.03 au).

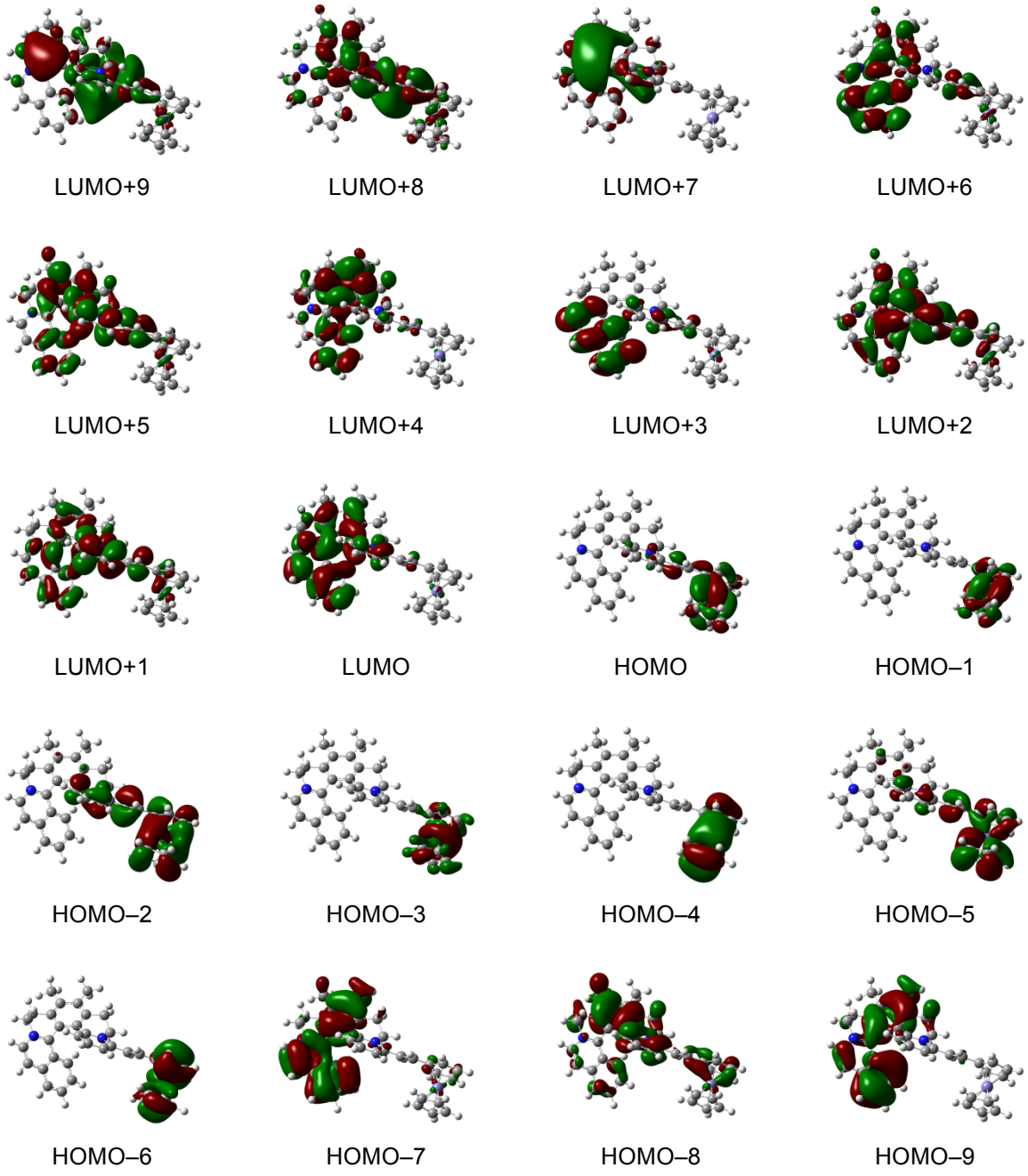

Fig. S17 PBE0/6-311++G(d)/LANL2DZ-derived contour surface diagrams of selected MOs for complex **3** (isosurface value 0.03 au).

Table S4 Contributions (%) of various fragments to the frontier MOs computed by PBE0/6-311++G(d)/LANL2DZ for complexes 1–3

	1					**2**					**3**				
	C_5H_5	Fe	C_5H_4	CH=CH	Hq	C_5H_5	Fe	C_5H_4	CH=CH	Hq	C_5H_5	Fe	C_5H_4	CH=CH	Hq
LUMO+12	11	21	31	11	26	3	8	17	10	65	6	17	10	9	58
LUMO+11	13	24	27	4	32	19	41	18	0	22	15	34	20	1	30
LUMO+10	11	22	12	0	56	13	1	11	8	67	7	0	10	11	72
LUMO+9	7	2	6	2	83	3	3	5	13	76	1	4	9	12	74
LUMO+8	4	6	3	4	83	7	12	5	16	60	5	6	28	24	37
LUMO+7	5	11	5	21	59	2	0	7	10	81	1	1	7	11	81
LUMO+6	2	1	10	7	80	1	1	1	3	94	1	1	3	8	87
LUMO+5	1	2	1	11	86	1	2	1	15	81	1	2	2	10	85
LUMO+4	0	1	0	4	95	0	0	0	0	100	0	0	0	1	99
LUMO+3	0	1	1	3	95	0	1	2	3	94	0	0	0	2	98
LUMO+2	1	3	2	9	86	0	0	0	2	98	1	3	3	10	83
LUMO+1	1	3	2	9	86	2	4	3	14	77	1	3	2	10	84
LUMO	0	1	1	4	94	0	1	1	3	95	0	0	0	1	98
HOMO	6	75	7	6	6	6	75	7	6	6	6	80	8	3	3
HOMO–1	7	86	7	0	0	7	86	7	0	0	7	86	7	0	0
HOMO–2	20	28	28	11	13	19	26	29	12	13	30	6	35	15	15
HOMO–3	13	67	17	1	1	12	71	14	2	1	9	73	14	4	0
HOMO–4	69	2	29	0	0	68	2	30	0	0	68	2	30	0	0
HOMO–5	52	27	12	4	5	54	26	11	4	4	47	27	16	3	7
HOMO–6	15	28	57	0	0	16	28	56	0	0	16	28	56	0	0
HOMO–7	0	0	0	0	100	0	0	0	0	100	0	1	2	0	97
HOMO–8	0	0	1	1	98	0	0	0	0	100	0	2	7	0	91
HOMO–9	2	5	38	31	24	0	0	1	0	99	0	0	1	0	99
HOMO–10	0	0	0	0	100	2	5	39	30	24	1	3	25	24	46
HOMO–11	39	11	32	3	15	0	0	0	0	99	0	0	2	4	93
HOMO–12	3	0	5	2	89	0	0	0	0	100	5	2	9	12	72

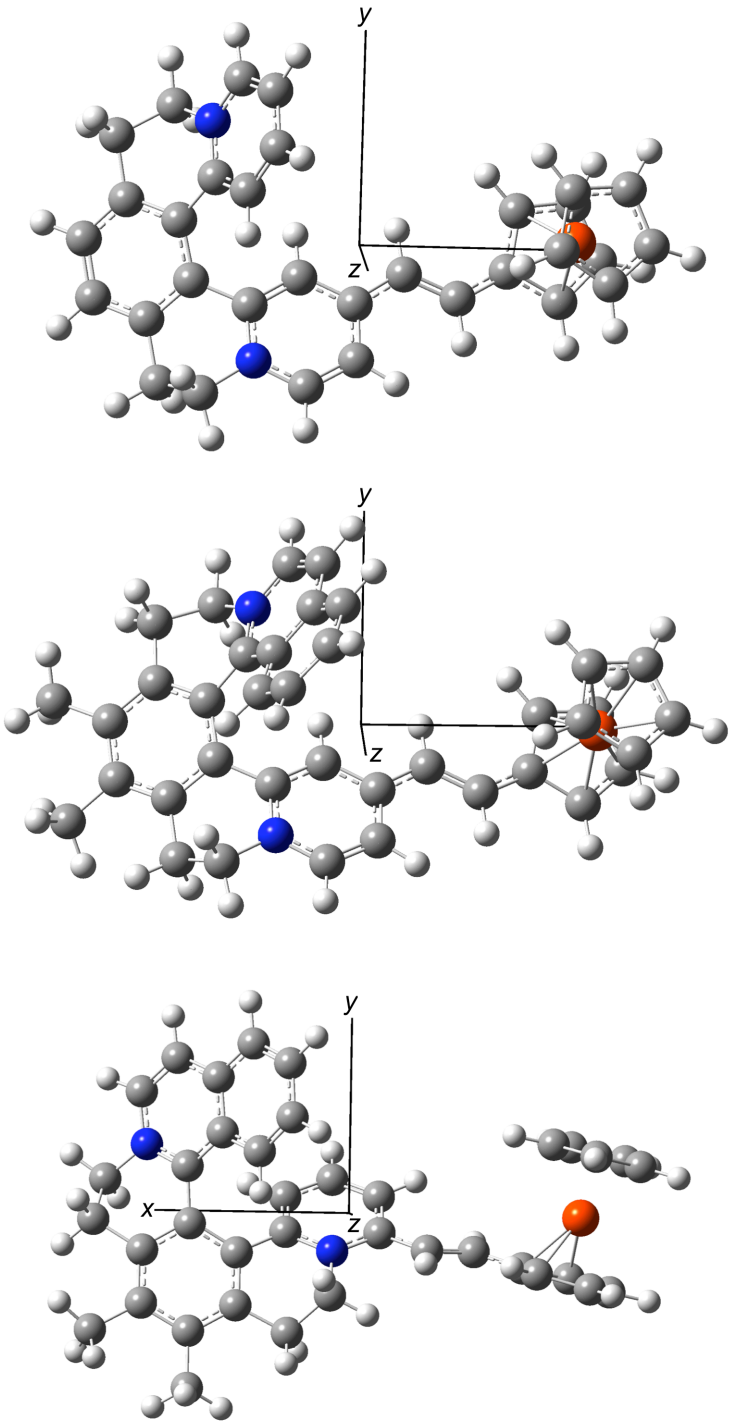

Fig. S18 Optimised molecular structures and the axis labeling used in the DFT calculations for complexes **1**–**3**.

Table S5 Geometric parameters for the PBE0/6-311++G(d)/LANL2DZ-optimised structures of the cations $\mathbf{2}^{2+}$ and $\mathbf{2}^{\cdot 3+}$

	distances (Å)			angles (°)[a]	
	$\mathbf{2}^{2+}$	$\mathbf{2}^{\cdot 3+}$		$\mathbf{2}^{2+}$	$\mathbf{2}^{\cdot 3+}$
C1–C2	1.422	1.454	C1–C2–C3	126.2	124.8
C2–C3	1.366	1.346	C2–C3–C4	125.1	124.1
C3–C4	1.424	1.460	θ (A/B)	59.8	64.1
Fe–C(C_5H_4)	2.030–2.066	2.062–2.098	θ (A/D)	16.1	49.3
Fe–C(C_5H_5)	2.045–2.055	2.069–2.070	θ (A/C)	7.24	22.3
			θ (C/D)	10.4	27.0

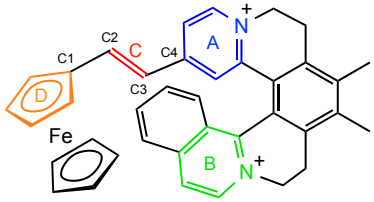

[a] θ denotes the dihedral angles between the least-squares planes defined by the colour-coded fragments A–D.

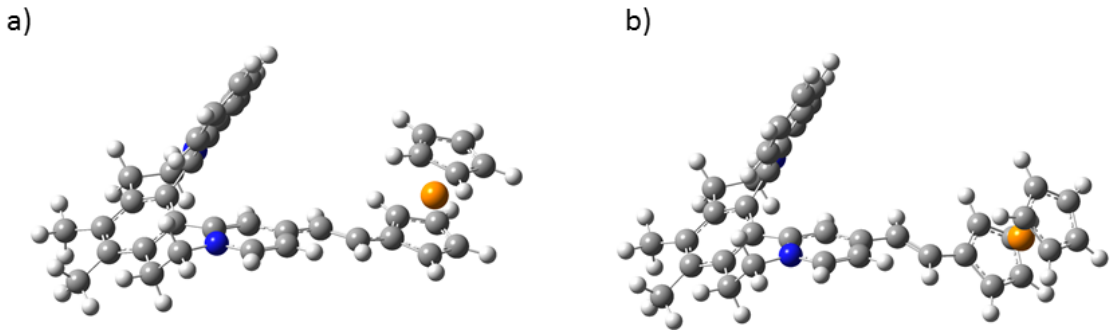

Fig. S19 Views of the PBE0/6-311++G(d)/LANL2DZ-optimised geometries of the cations $\mathbf{2}^{2+}$ (a) and $\mathbf{2}^{\cdot 3+}$ (b).

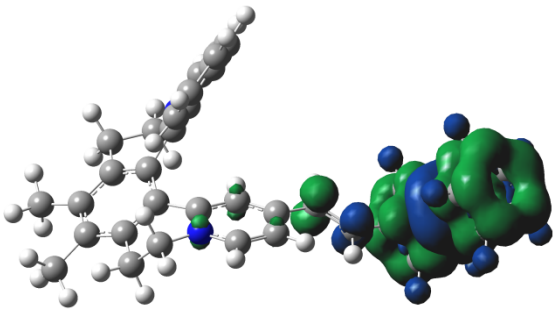

Fig. S20 Spin density plot (PBE0/6-311++G(d)/LANL2DZ) for the cation $\mathbf{2}^{\cdot 3+}$.

Table S6 Selected TD-DFT-calculated data for $2^{\cdot 3+a}$

no.	$\lambda_{max,exp}$ [b] (nm)	$\lambda_{max,calc}$ [c] (nm)	λ_{calc} [d] (nm)	E_{calc} (eV)	f_{os}	main contributions (weight)
1	486		503	2.46	0.010	H–2(α) → L(α) (20%), H–11(β) → L(β) (10%), H–4(β) → L(β) (8%), H–4(β) → L+1(β) (6%), H–1(β) → L+1(β) (8%)
2	451	429	445	2.79	0.029	H–6(α) → L+2(α) (32%), H–3(β) → L+4(β) (15%), H–7(α) → L(A) (7%), H–8(β) → L(β) (6%)
3			409	3.03	0.023	H(α) → L(α) (11%), H–6(β) → L(β) (56%), H(β) → L(β) (14%)
4			408	3.04	0.069	H(α) → L(α) (21%), H–6(β) → L(β) (30%), H(β) → L(β) (28%), H(β) → L+1(β) (12%)
5			398	3.12	0.059	H(α) → L(α) (17%), H(β) → L(β) (40%), H(β) → L+1(β) (14%)
6			396	3.13	0.011	H–12(α) → L+2(α) (9%), H–10(β) → L+4(β) (9%), H–11(α) → L(α) (7%), H–2(α) → L+3(α) (6%),
7	375	378	383	3.24	0.371	H–1(α) → L(α) (33%), H–2(β) → L(β) (16%), H–2(β) → L+1(β) (15%), H–1(β) → L+1(β) (14%)
8			378	3.28	0.042	H(α) → L+1(α) (11%), H–2(β) → L(β) (13%), H–2(β) → L+2(β) (11%), H(β) → L+1(β) (11%)
9			368	3.37	0.153	H–2(α) → L(α) (21%), H–2(α) → L+1(α) (7%), H–2(β) → L+1(β) (6%)
10			365	3.40	0.011	H–2(β) → L(β) (17%), H–2(β) → L+1(β) (8%), H(β) → L+6(β) (8%)
11			361	3.43	0.011	H–1(α) → L+1(α) (21%), H–2(β) → L(β) (12%), H(α) → L+5(α) (7%), H(β) → L+6(β) (6%)
12			349	3.55	0.097	H(α) → L+1(α) (24%), H(β) → L+2(β) (40%), H–1(β) → L+1(β) (6%)
13	348	349	347	3.57	0.126	H–1(β) → L+1(β) (15%), H(β) → L+2(β) (17%), H–2(β) → L+1(β) (8%), H–2(α) → L+1(α) (7%)
14			339	3.66	0.075	H–2(α) → L(α) (11%), H–2(α) → L+1(α) (12%), H–4(β) → L+1(β) (18%), H–3(α) → L(α) (6%)
15			335	3.70	0.020	H–3(α) → L(α) (16%), H–2(β) → L+2(β) (13%), H–5(β) → L+1(β) (9%), H–4(α) → L+2(α) (8%), H–5(β) → L(β) (8%)
16			334	3.71	0.023	H–4(α) → L+2(α) (11%), H–5(β) → L(β) (12%), H–2(β) → L+2(β) (8%), H–7(β) → L+1(β) (6%)

17			333	3.72	0.015	H–3(α) → L(α) (22%), H–1(α) → L+1(α) (14%), H–2(β) → L+2(β) (15%)
18			331	3.75	0.103	H–4(α) → L+2(α) (27%), H–5(β) → L(β) (21%), H–2(α) → L+1(α) (8%)
19			328	3.78	0.059	H–4(α) → L+2(α) (10%), H–3(α) → L(α) (11%), H–5(β) → L+1(β) (8%), H–5(β) → L(β) (7%)
20			323	3.84	0.015	H–5(β) → L(β) (14%), H–4(β) → L+1(β) (15%), H–1(β) → L+2(β) (16%)
21			322	3.85	0.012	H–5(β) → L(β) (11%), H–5(β) → L+1(β) (18%), H–1(β) → L+2(β) (11%)
22			320	3.87	0.024	H–12(α) → L+2(α) (16%), H–10(β) → L+4(β) (11%), H–4(β) → L+1(β) (16%), H–5(β) → L+1(β) (8%)
23	322	319	313	3.96	0.184	H–2(α) → L+1(α) (18%), H–1(β) → L+2(β) (14%), H–9(β) → L+1(β) (5%)
24			308	4.03	0.131	H–2(α) → L+1(α) (16%), H–2(α) → L+3(α) (9%), H–9(β) → L+1(β) (9%), H–9(α) → L(α) (6%),
25			301	4.12	0.016	H–3(α) → L+1(α) (37%), H–5(β) → L+2(β) (23%), H–3(α) → L(α) (8%)

[a] Geometry optimisations and TD-DFT calculations used the PBE0 functional with the 6-311++G(d)/LANL2DZ mixed basis set, and a CPCM MeCN solvent model was included for TD-DFT. Only the transitions with $f_{os} \geq 0.01$ are included. H = HOMO, L = LUMO. [b] Measured by *in situ* spectroelectrochemistry of a MeCN solution ca. 10^{-4} M in [**2**][TfO]$_2$ and 0.1 M in [N(C$_4$H$_9$-*n*)$_4$]PF$_6$ at 293 K in an OTTLE cell. [c] Obtained from the simulated absorption spectrum. [d] For the individual calculated electronic transitions.

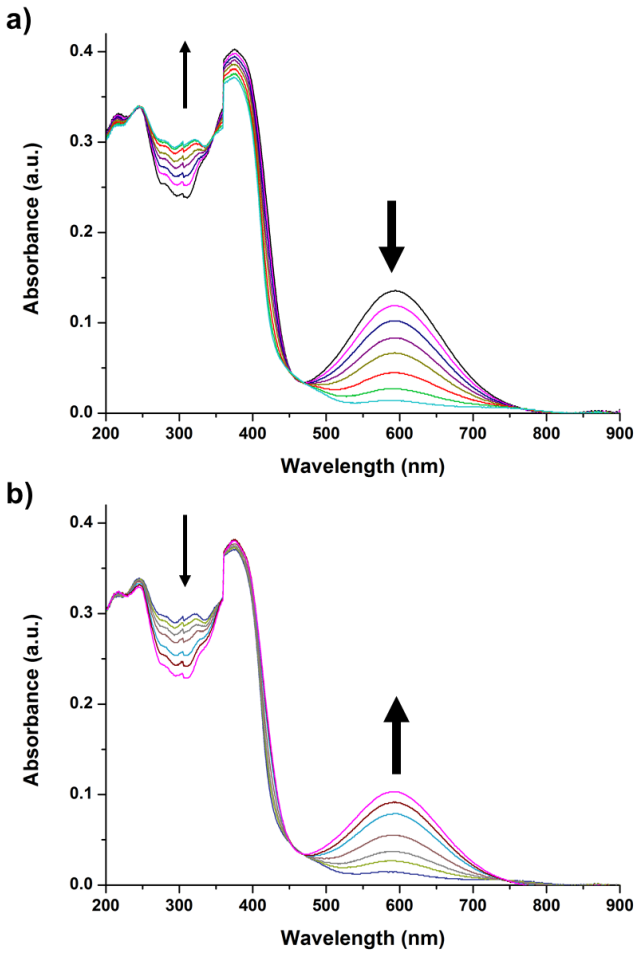

Fig. S21 Spectroscopic changes upon oxidation at 0.5 V vs FcH^+/FcH (a) followed by reduction at –0.5 V (b) of complex salt [**2**][TfO]$_2$ (ca. 10^{-4} M) in MeCN 0.1 M in [N(C_4H_9-*n*)$_4$]PF_6 at 293 K in an OTTLE cell.

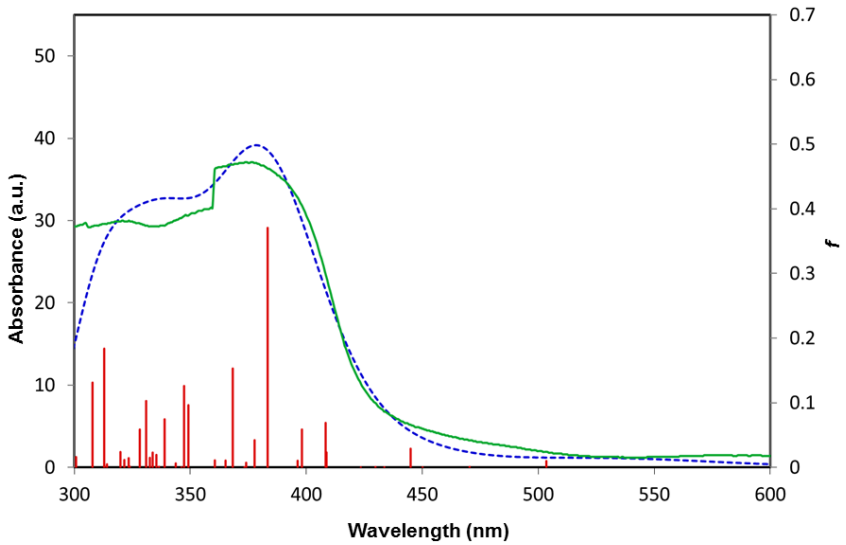

Fig. S22 Experimental UV–vis spectrum of $\mathbf{2}^{\cdot 3+}$ (green) measured by spectroelectrochemistry of a MeCN (ca. 10^{-4} M) solution 0.1 M in [N(C_4H_9-*n*)$_4$]PF_6 at 293 K in an OTTLE cell, together with the PBE0/6-311++G(d)/LANL2DZ-calculated spectrum (blue dashed).

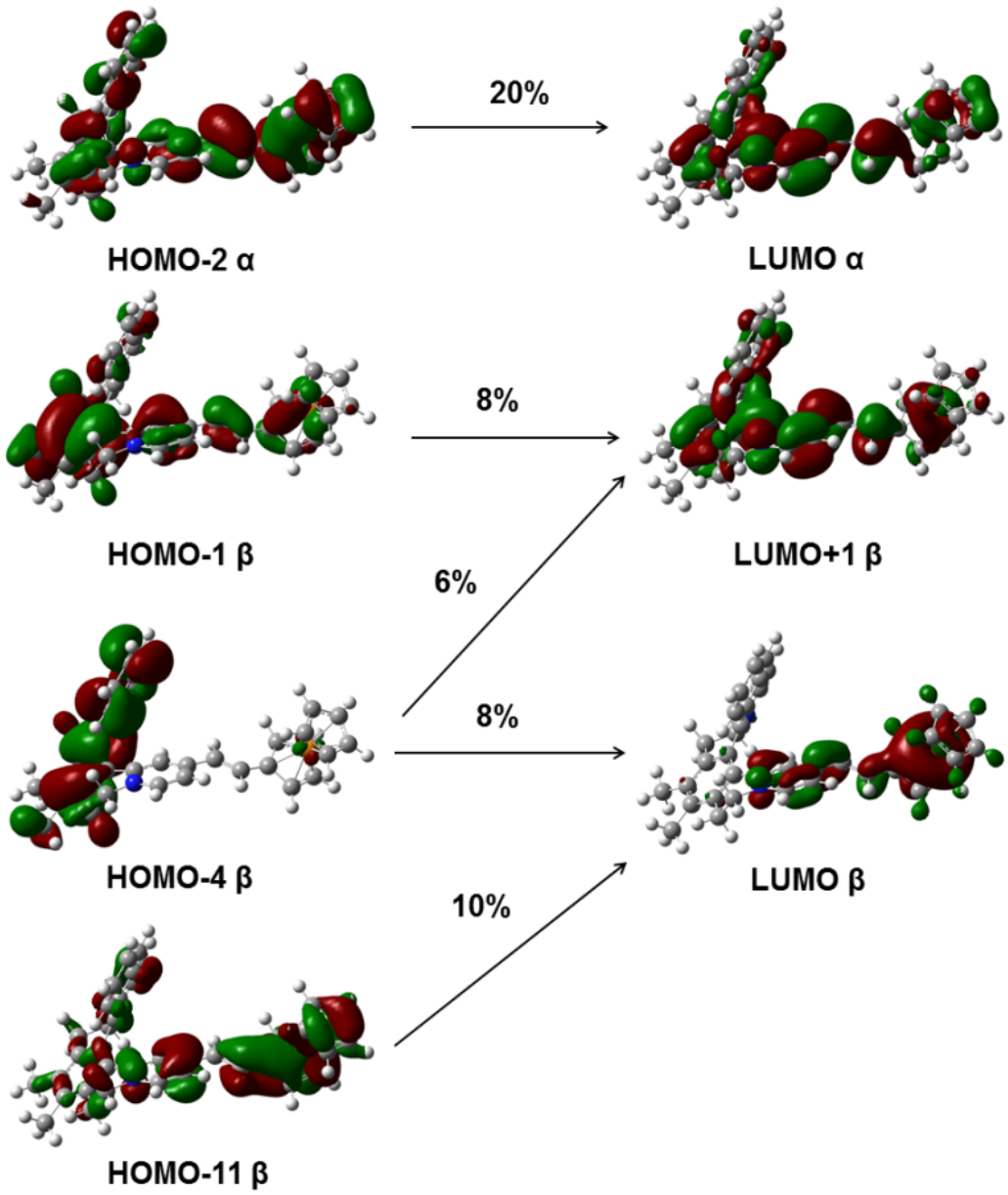

Fig. S23 PBE0/6-311++G(d)/LANL2DZ-derived contour surface diagrams of MOs involved in the computed transition at 503 nm for the cation $\mathbf{2}^{\cdot 3+}$.

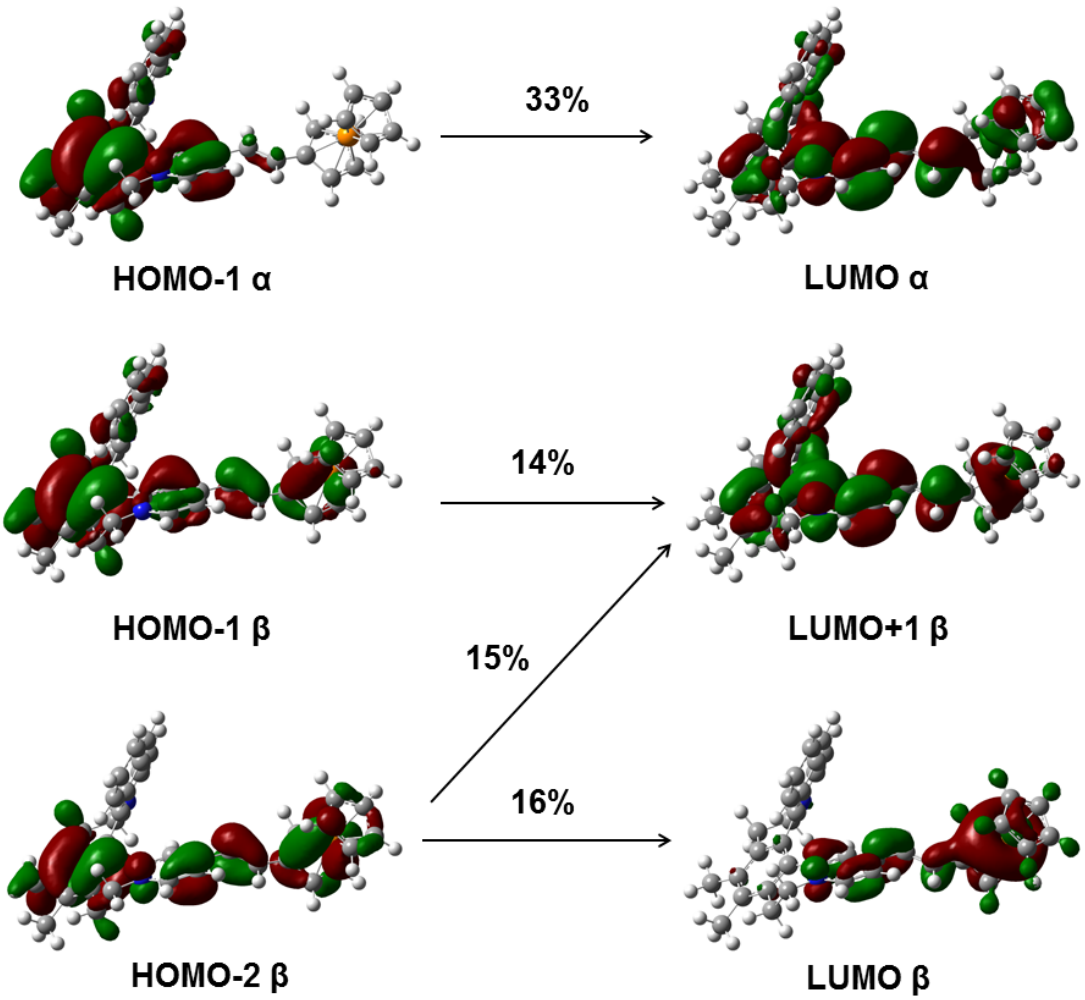

Fig. S24 PBE0/6-311++G(d)/LANL2DZ-derived contour surface diagrams of MO involved in the computed transition at 375 nm for the cation $\mathbf{2}^{\cdot 3+}$.

Table S7 Static first hyperpolarizabilities (10^{-30} esu) calculated at the PBE0/6-311++G(d)/LANL2DZ level for $\mathbf{2}^{\cdot 3+}$

complex	β_{xxx}	β_{xxy}	β_{xyy}	β_{yyy}	β_{xxz}	β_{xyz}	β_{yyz}	β_{xzz}	β_{yzz}	β_{zzz}	β_{x}	β_{y}	β_{z}	β_{tot}
$\mathbf{2}^{\cdot 3+}$ [a]	–22.3	–10.9	5.3	6.1	19.8	0.4	1.9	1.0	–0.5	–0.6	–15.9	–5.3	21.1	27
$\mathbf{2}^{\cdot 3+}$ [b]	–22.4	–15.8	11.5	16.4	38.9	2.4	5.0	2.0	–1.5	–3.2	–8.9	–0.9	40.7	42

[a] In the gas phase. [b] In MeCN.